Bio-Design and Manufacturing (2024) 7:105–120
https://doi.org/10.1007/s42242-023-00264-0

RESEARCH ARTICLE

Ag-doped CNT/HAP nanohybrids in a PLLA bone scaffold show significant antibacterial activity

Cijun Shuai[1,2,3] · Xiaoxin Shi[1] · Kai Wang[1] · Yulong Gu[1] · Feng Yang[1] · Pei Feng[1]

Received: 22 June 2023 / Accepted: 7 December 2023 / Published online: 27 February 2024

Abstract

Bacterial infection is a major problem following bone implant surgery. Moreover, poly-L-lactic acid/carbon nanotube/hydroxyapatite (PLLA/CNT/HAP) bone scaffolds possess enhanced mechanical properties and show good bioactivity regarding bone defect regeneration. In this study, we synthesized silver (Ag)-doped CNT/HAP (CNT/Ag-HAP) nanohybrids via the partial replacing of calcium ions (Ca^{2+}) in the HAP lattice with silver ions (Ag^{+}) using an ion doping technique under hydrothermal conditions. Specifically, the doping process was induced using the special lattice structure of HAP and the abundant surface oxygenic functional groups of CNT, and involved the partial replacement of Ca^{2+} in the HAP lattice by doped Ag^{+} as well as the in situ synthesis of Ag-HAP nanoparticles on CNT in a hydrothermal environment. The resulting CNT/Ag-HAP nanohybrids were then introduced into a PLLA matrix via laser-based powder bed fusion (PBF-LB) to fabricate PLLA/CNT/Ag-HAP scaffolds that showed sustained antibacterial activity. We then found that Ag^{+}, which possesses broad-spectrum antibacterial activity, endowed PLLA/CNT/Ag-HAP scaffolds with this activity, with an antibacterial effectiveness of 92.65%. This antibacterial effect is due to the powerful effect of Ag^{+} against bacterial structure and genetic material, as well as the physical destruction of bacterial structures due to the sharp edge structure of CNT. In addition, the scaffold possessed enhanced mechanical properties, showing tensile and compressive strengths of 8.49 MPa and 19.72 MPa, respectively. Finally, the scaffold also exhibited good bioactivity and cytocompatibility, including the ability to form apatite layers and to promote the adhesion and proliferation of human osteoblast-like cells (MG63 cells).

✉ Pei Feng
fengpei@csu.edu.cn

1 State Key Laboratory of Precision Manufacturing for Extreme Service Performance, College of Mechanical and Electrical Engineering, Central South University, Changsha 410083, China

2 Institute of Additive Manufacturing, Jiangxi University of Science and Technology, Nanchang 330013, China

3 College of Mechanical Engineering, Xinjiang University, Urumqi 830017, China

Graphic abstract

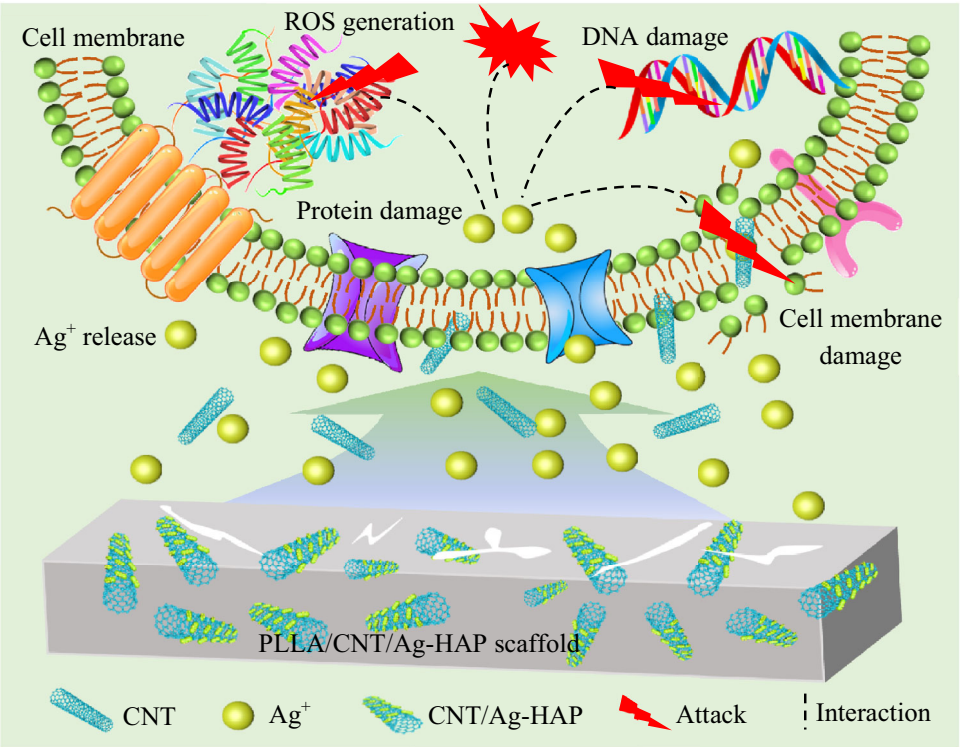

Keywords Ag-doped · Carbon nanotube/hydroxyapatite (CNT/HAP) · Antibacterial properties · Bone scaffold

Introduction

Artificial bone scaffolds perform an extremely important role by acting as a bone substitute during the transplantation and repair of bone defects [1–3]. The combination of carbon nanotubes (CNTs) and hydroxyapatite (HAP), especially the in situ synthesis of HAP nanoparticles on CNTs (termed CNT/HAP), has been found to improve the mechanical properties and bioactivity of biopolymer bone scaffolds [4–6]. Nevertheless, numerous clinical studies have shown that artificial bone scaffolds may cause serious bacterial infections when transplanted into the human body, and this can undermine the intended function of bone scaffolds, causing the implantation procedure to fail, or even causing amputation in severe cases [7, 8]. Therefore, it is imperative to develop an antibacterial strategy to endow bone scaffolds with antibacterial properties to prevent bacterial infection from bone implants.

Toward this end, bone scaffolds loaded with antibiotics have been developed. However, the overuse of antibiotics has given rise to the increasing incidence of multidrug-resistant bacteria, whose infections have become a serious threat to human health [9]. Currently, inorganic antimicrobial agents, including silver (Ag), copper (Cu), and zinc (Zn), as well as other nanometals and their ions, have become important for antibiotic research since they are less likely to induce drug resistance [10, 11]. However, it has also been found that composite scaffolds directly loaded with Ag nanoparticles and/or other antibacterial nanometals not only weaken antibacterial activity but can also cause burst releases of nanoparticles that fail to generate sustained antibacterial activity. This is thought to be due to the strong surface energy of nanometals and their incompatibility with the polymer matrix [12, 13]. However, doping procedures using antibacterial metal ions can compensate for this effect via altering the crystal structures of substances, thereby obtaining sustained antibacterial activity [14, 15]. Thus, it would be desirable to achieve the continuous release of antibacterial substances from scaffolds by doping antibacterial metal ions into the CNT/HAP crystal structure [16].

HAP ($Ca_{10}(PO_4)_6(OH)_2$) is a hexagonal crystal system that includes two types of Ca^{2+} in different positions within its unit cell. This special structural composition, which includes different valence bonds and radii of Ca^{2+}, provides HAP with a strong ion exchange ability [17, 18]. It has been shown that the Ca^{2+} ions within the HAP lattice can

be replaced by metal ions with different valences and radii, including Ag^+, potassium ions (K^+), and zinc ions (Zn^{2+}), among others [15]. Of these, Ag^+ is recognized as a strong antibacterial agent capable of combating both Gram-positive and Gram-negative bacteria. It can be used to fight against many bacterial infections both in vitro and in vivo and therefore is widely used in studies related to the antibacterial functions of bone scaffolds [19, 20]. More importantly, Ag^+ has a radius size that is similar to Ca^{2+}. Moreover, the abundant negatively charged carboxyl and epoxy groups present on the surface of carboxylated CNT can trap Ag^+ in solution via electrostatic interactions. Both may provide convenient conditions for Ag^+ to enter into the HAP lattice and partially replace Ca^{2+} [21, 22]. In addition, Ag^+ is known to display good biocompatibility and be non-toxic to cells at low concentrations [23]. Therefore, it is reasonable to develop a strategy whereby the Ca^{2+} in the HAP lattice is replaced by Ag^+, thereby endowing the scaffold with sustained antibacterial properties.

In the present work, we grew Ag-doped HAP nanohybrids with efficient antibacterial properties in situ on CNT via partial replacement of the Ca^{2+} ions in the HAP lattice with Ag^+ under hydrothermal conditions. We did so by combining silver nitrate ($AgNO_3$), calcium nitrate tetrahydrate extra pure ($Ca(NO_3)_2{\cdot}4H_2O$), diammonium hydrogen phosphate ($(NH_4)_2HPO_4$), and CNT in a vessel. Next, the Ag-doped CNT/HAP (CNT/Ag-HAP) nanohybrids were first introduced into poly-L-lactic acid (PLLA), and a PLLA/CNT/Ag-HAP antibacterial scaffold with a porous structure was prepared using a laser-based powder bed fusion (PBF-LB) technique. We also report the construction process and the doping mechanism of the CNT/Ag-HAP nanohybrids. Likewise, the macrostructures, microstructures, and mechanical properties of PLLA/CNT/Ag-HAP scaffolds were comprehensively studied. More importantly, we evaluated the antibacterial properties of the hybrids by inhibition zone and turbidimetry tests, and elucidated the antibacterial mechanism involved. In addition, the bioactivity of the scaffold was researched using an in vitro immersion test. Finally, cytocompatibility was assessed using cell adhesion and proliferation tests.

Materials and methods

Materials

PLLA powder (molecular weight: 100 kDa; purity >98%) was obtained from Jinan Daigang Biomaterial Co., Ltd. (China). CNTs were obtained from Nanjing XFNANO Materials Techn Co., Ltd. (China). CNTs showed a carboxyl group content of 2.56% (mass fraction), a length range of 30–50 μm, and a diameter range of 15–50 nm. $(NH_4)_2HPO_4$ and $Ca(NO_3)_2{\cdot}4H_2O$ were obtained from Sinopharm Chemical Reagent Co., Ltd. (China). Ammonium water (NH_4OH) was obtained from Guangdong Guanghua Sci-Tech Co., Ltd. (China). $AgNO_3$ was obtained from the Shanghai Institute of Fine Chemical Materials (China).

Synthesis of CNT/Ag-HAP

CNT/Ag-HAP nanohybrids were synthesized using an in situ growth protocol. The synthetic process to CNT/Ag-HAP was as follows. First, 50 mg CNT powder was dispersed in distilled water, and ultrasonic stirring was performed for 30 min to obtain a uniformly dispersed suspension. Second, 0.75 g $(NH_4)_2HPO_4$ powder and 2.13 g $Ca(NO_3)_2{\cdot}4H_2O$ powder were added to distilled water, respectively. Next, 0.08 g $AgNO_3$ powder was added into the above $Ca(NO_3)_2{\cdot}4H_2O$ solution, and this mixture was then slowly added to the prepared CNT suspension under continued stirring for 2 h. Next, an $(NH_4)_2HPO_4$ solution was slowly dripped into the well-mixed suspension, and the pH was raised to approximately 10 by addition of an NH_4OH solution. Here, $AgNO_3$, $Ca(NO_3)_2{\cdot}4H_2O$, and $(NH_4)_2HPO_4$ were the sources of Ag, Ca, and phosphorus (P), respectively. Next, the resulting mixture was poured into a Teflon-lined hydrothermal autoclave to generate a hydrothermal reaction under a vacuum at 120 °C for 24 h. Finally, CNT/Ag-HAP nanohybrids were obtained by centrifugation, washing, and drying of the resulting suspension. For comparison, CNT/HAP nanohybrids were synthesized under the same conditions without the addition of the $AgNO_3$ solution.

Analysis of CNT/Ag-HAP

The crystal structure of the nanohybrids was examined using an X-ray diffractometer (XRD, New Empyrean Co., Ltd., Netherlands) at a speed of 5 °/min. Fourier transform infrared spectroscopy (FTIR, Tianjin Gangdong Sci.&Tech. Co., Ltd., China) was then performed to evaluate the functional groups of the nanohybrids. Next, X-ray photoelectron spectroscopy (XPS, Thermo Fisher Scientific, USA) was used to study the elemental composition of the nanomaterial, and peak separation was analyzed using Avantage software. Scanning electron microscopy (SEM, Phenom-World BV, Netherlands) and transmission electron microscopy (TEM, Thermo Fisher Scientific, USA) were performed to study the Ag^+ doping process. Finally, the distribution of elements was detected via an energy-dispersive spectrometer (EDS) equipped on SEM.

Scaffold fabrication

PBF-LB is a common additive manufacturing (AM) technology that uses laser energy to fuse together particulate

materials, such as metals, ceramics, or polymers, to form three-dimensional objects [24, 25]. Common PBF-LB techniques include selective laser sintering (SLS), selective laser melting, and electron beam melting. Of these, SLS is mainly employed to help form polymer powders [26, 27]. In this study, a self-developed SLS system was employed to construct a scaffold layer by layer [28]. First, CNT/Ag-HAP powder (12%, mass fraction) and PLLA powder (88%, mass fraction) were separately dispersed into deionized water and mixed together after stirring and ultrasonic processing at ambient temperature. Next, the composite powder after drying and grinding was spread onto a powder spreading platform. For SLS, the laser power was set to 3.5 W, the scanning speed was set to 120 mm/s, and the powder spreading platform moved down by the height of one powder layer after each scan. The above process was repeated until all powder layers were sintered, and all unsintered powder was removed to obtain a composite scaffold. Constructed porous scaffolds were labeled as PLLA, PLLA/CNT, PLLA/CNT/HAP, and PLLA/CNT/Ag-HAP.

Scaffold microstructure and mechanical properties

The surface macrostructure and surface and cross-sectional microtopography of the PLLA, PLLA/CNT, PLLA/CNT/HAP, and PLLA/CNT/Ag-HAP scaffolds were studied by digital photography and SEM to analyze the dispersion of CNT in the polymer matrix. For this analysis, all scaffolds were sprayed with gold to improve conductivity. Mechanical property tests, including tension and compression tests, were performed under uniaxial load using a universal testing machine (Jinan Zhongluchang Testing Machine Manufacturing Co., Ltd., China). During testing, the loading speed was 0.5 mm/min. Each set of scaffolds was measured five times to generate a mean and standard deviation. Finally, the modulus and strength were calculated using stress–strain curves.

Antibacterial properties of scaffolds

Elevated levels of reactive oxygen species (ROS) have been found to be a crucial factor in bacterial apoptosis. We therefore assessed ROS generation caused by the PLLA/CNT/Ag-HAP scaffolds. Specifically, the superoxide ($\cdot O_2^-$) radical and hydroxyl ($\cdot$OH) radical produced by the PLLA/CNT/Ag-HAP scaffold sample were identified using an electron paramagnetic resonance (EPR) spectrometer (EMXplus-6/1, Bruker, Germany) with 5,5-dimethyl-1-pyrroline-N-oxide (DMPO, 0.1 mol/L) used as the trapping agent. The antibacterial properties of scaffolds against *Escherichia coli* (*E. coli*) were evaluated using an inhibition zone test. First, a bacterial suspension of *E. coli* at a concentration of 1×10^6 CFU/mL (CFU: colony forming units) was configured, and then spread evenly on an agar culture plate. Next, after ultraviolet (UV) irradiation for sterilization, the scaffold was inserted in the center of the culture plate and cultured on a shaker at 37 °C for 24 h. Finally, a digital camera was used to record the inhibition zone around the scaffold.

Next, antibacterial properties were further quantitatively analyzed using turbidimetry. To do so, the scaffolds were first sterilized using UV light before testing. Moreover, a test tube containing culture medium but no bacteria or scaffold was used as a blank control group, a test tube containing culture medium and bacteria but no scaffold was used as a negative control group, while test tubes containing culture medium, bacteria, and one of the scaffolds were used as experimental groups. Different scaffolds were immersed in test tubes containing a bacterial suspension (1×10^6 CFU/mL), and all test tubes were maintained at approximately 37 °C for 24 h. Next, the test tubes were photographed using a digital camera for turbidity contrast analysis. In addition, the absorbance at 600 nm was assessed using an enzyme-labeled instrument (Thermo Fisher Scientific, USA). The antibacterial rate was calculated according to formula [29]:

$$\text{Antibacterial rate} = (B - A - C)/(B - A) \times 100\%,$$

where A represents the absorbance of the bacterial suspension in the blank control group, B represents the absorbance of the bacterial suspension in the negative control group, and C represents the absorbance of the bacterial suspension in the experimental group. In addition, the morphology of bacteria on the scaffold surface was examined after 24 h of culture. All scaffolds were fixed with 2.5% glutaraldehyde for 24 h and then dehydrated with gradient ethanol solutions (30%, 50%, 70%, 90%, and 100%) for 15 min. Finally, all dried scaffolds were observed by SEM.

Scaffold bioactivity and cytocompatibility

Next, the mineralization ability of PLLA/CNT/Ag-HAP scaffolds was evaluated using an in vitro immersion test. Briefly, the scaffold was immersed in 50 mL of simulated body fluid (SBF) solution, and the solution was changed every 2 days. The scaffold was removed after 28 d, rinsed three times with distilled water, and then dried for 1 d. The surface morphology of the scaffold was examined by SEM. Subsequently, the cytocompatibility of human osteoblast-like cells (MG63 cells, American Type Culture Collection, USA) was assessed by adhesion and fluorescence experiments on the scaffold. All scaffolds were then disinfected with UV light for 30 min, after which MG63 cells (1×10^5 cells/mL) were inoculated onto the surface of each scaffold and then cultured in Dulbecco's modified eagle medium for 1, 3, and 5 d at 37 °C and 5% CO_2. The cell adhesion morphology of the MG63 cells was observed, and the relative

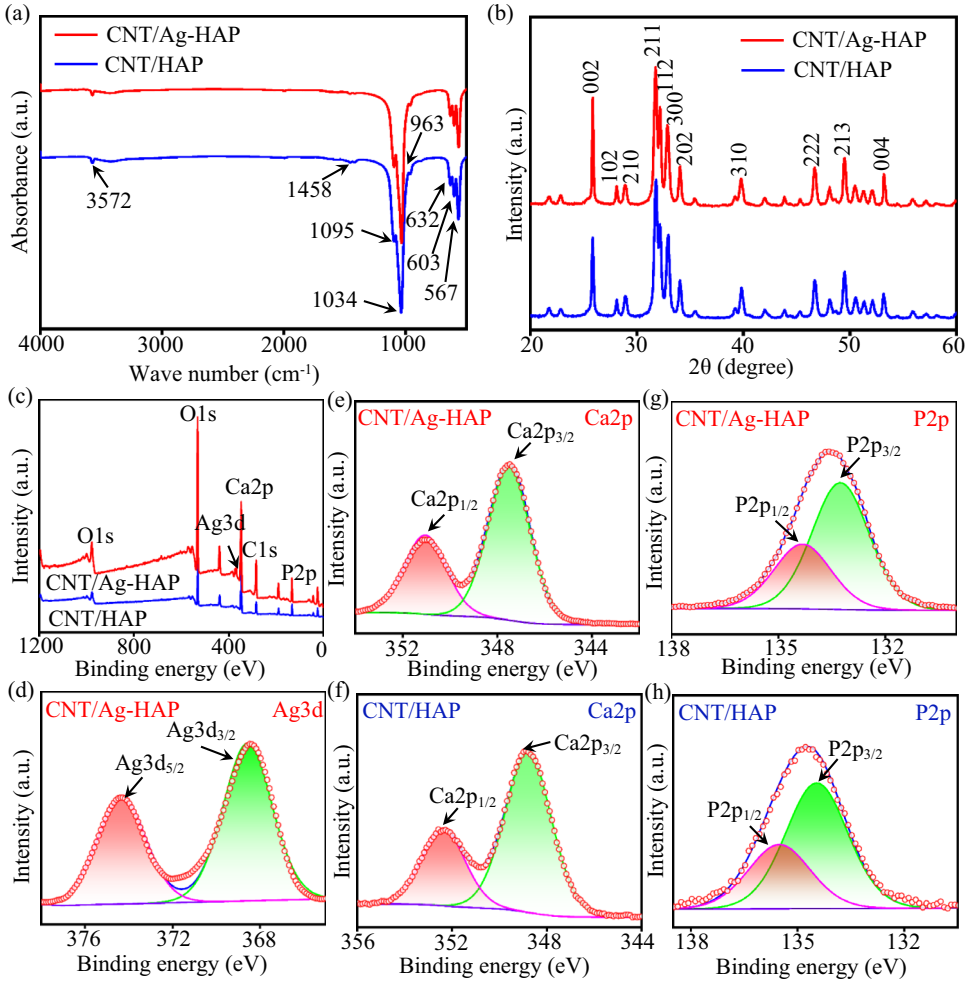

Fig. 1 Characterization of CNT/HAP and CNT/Ag-HAP nanohybrids: **a** FTIR spectra, **b** XRD spectra, and **c**–**h** XPS spectra. CNT: carbon nanotube; HAP: hydroxyapatite; CNT/Ag-HAP: Ag-doped CNT/HAP; FTIR: Fourier transform infrared spectroscopy; XRD: X-ray diffractometer; XPS: X-ray photoelectron spectroscopy

area of cells was calculated for each culture period. Finally, we conducted a fluorescence experiment in which the cells on the scaffold were stained with calcein acetoxymethyl ester (calcein-AM) and propidium iodide and the cell density was calculated. We then used a fluorescence microscope (Olympus, Japan) and found that the living cells fluoresced green, while the dead cells fluoresced red.

Statistical analyses

Data are expressed as mean±standard deviation. Statistical significance was assessed by Statistic Package for Social Science software, with $^{*}p<0.05$ and $^{**}p<0.01$.

Results and discussion

Analysis of CNT/HAP and CNT/Ag-HAP

The functional groups of the CNT/HAP and CNT/Ag-HAP nanohybrids were analyzed by FTIR, as illustrated in Fig. 1a. These results show that the absorption peaks of the CNT/HAP and CNT/Ag-HAP nanohybrids were similar. Here, we found that strong absorption peaks at 3572 and 632 cm^{-1} corresponded to the stretching and bending vibration peaks of the –OH group, respectively. The absorption peaks at 1095, 1034, and 963 cm^{-1} represented the asymmetric stretching vibration peaks of P–O, and the absorption peaks at 603 and 567 cm^{-1} represented the bending vibration peaks of O–P–O. Compared to the standard peaks of HAP, all absorption peaks were in agreement with the standard peaks, indicating that both the CNT/HAP and CNT/Ag-HAP nanohybrids contained HAP [14]. We also noted that the absorption peak at 1458 cm^{-1} corresponded to CO_3^{2-}. This was attributed to the dissolution of a small amount of CO_2 in the solution, which produced CO_3^{2-} during the reaction. This in turn replaced a small amount of the PO_4^{3-} of HAP [30]. Next, when Ag^{+} was doped into the CNT/HAP nanohybrids, the peak of CO_3^{2-} was obviously weakened. This may be due to the calcium vacancy phenomenon caused by the substitution of Ca^{2+} by Ag^{+} within the HAP lattice. As a result,

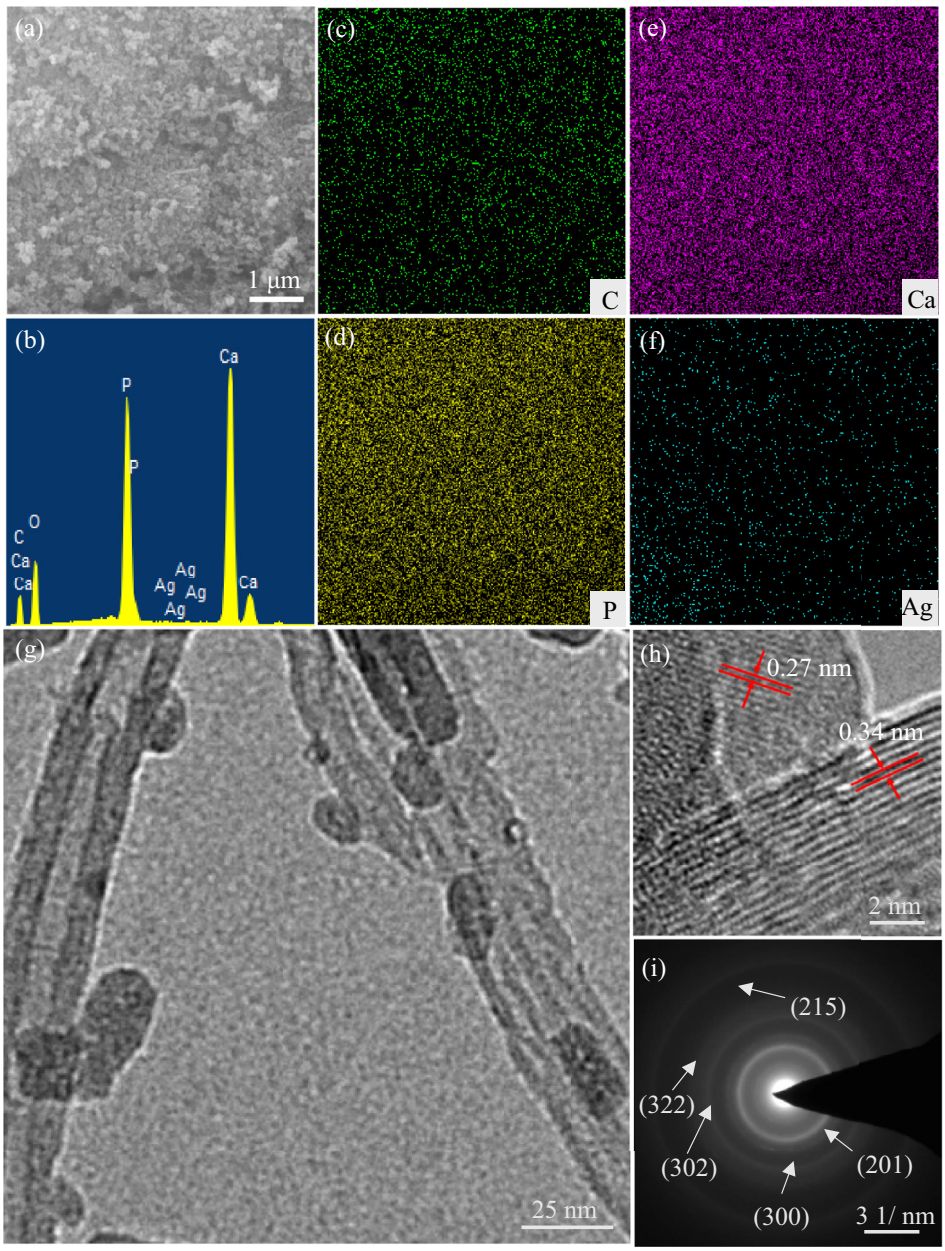

Fig. 2 Microstructure of the CNT/Ag-HAP nanohybrids: **a** SEM image, **b** EDS mapping spectra, **c–f** distribution of C, P, Ca, and Ag, **g** TEM image, **h** lattice spacing image, and **i** SAED image. CNT: carbon nanotube; HAP: hydroxyapatite; CNT/Ag-HAP: Ag-doped CNT/HAP; SEM: scanning electron microscopy; EDS: energy-dispersive spectrometer; TEM: transmission electron microscopy; SAED: selected area electron diffraction

the entry of CO_3^{2-} into the HAP lattice was hindered due to electrostatic repulsions [31].

The crystal structures of the CNT/HAP and CNT/Ag-HAP nanohybrids were then analyzed by XRD, as illustrated in Fig. 1b. We observed that the CNT/HAP and CNT/Ag-HAP nanohybrids displayed similar crystallographic properties. The diffraction peaks at 25.8°, 28.1°, 28.9°, 31.7°, 32.1°, 32.8°, 34.1°, 39.7°, 46.6°, 49.4°, and 53.2° corresponded to the crystal planes of (002), (102), (210), (211), (112), (300), (202), (310), (222), (213), and (004) in the HAP region, respectively. The absence of impurity peaks confirmed that the nanohybrids were pure HAP phase; this can be deduced by comparing with the standard card of HAP (JCPDS PDF No 09-0432). Furthermore, since Ag^+ was incorporated into the CNT/HAP nanohybrids, all peaks become sharp and their intensities were strong. This may be caused by the entry of Ag^+ into the primary lattice of HAP [14]. Next, the average microcrystalline sizes of the CNT/HAP and CNT/Ag-HAP nanohybrids were calculated using the XRD spectra and the Scherrer equation; these values were calculated to be 29 and 32 nm, respectively. These changes in lattice parameters may be due to the substitution of Ca^{2+} by Ag^+ within the HAP lattice or due to interstitial doping between the two phosphoric

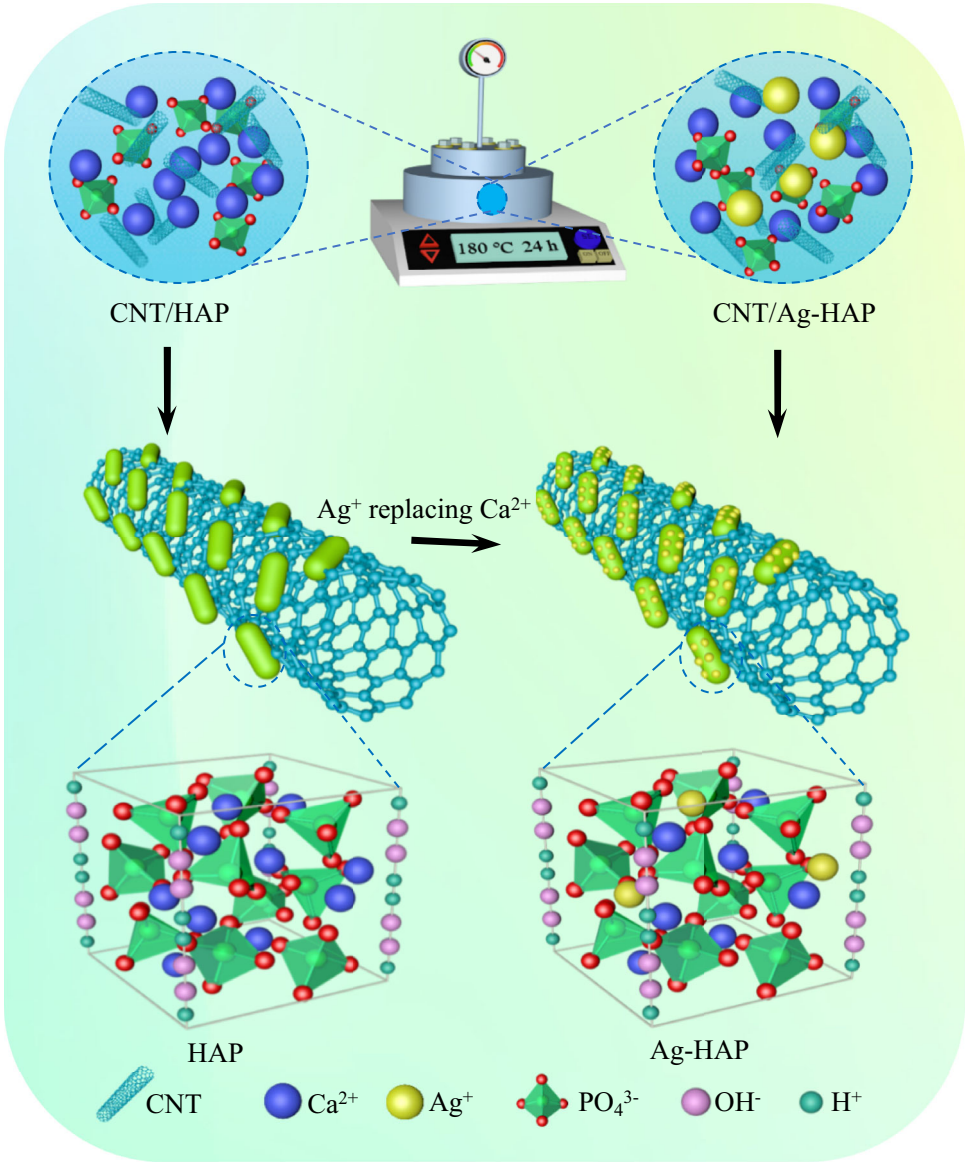

Fig. 3 Mechanism for partial replacement of Ca^{2+} in the HAP lattice by Ag^{+} to form CNT/Ag-HAP nanohybrids. CNT: carbon nanotube; HAP: hydroxyapatite; CNT/Ag-HAP: Ag-doped CNT/HAP

acid groups of HAP during ion exchange in solution. However, since the ionic radius of Ag^{+} (1.26 Å, 1 Å=10^{-10} m) was slightly larger than that of Ca^{2+} (0.99 Å), it would be easier for Ag^{+} to replace Ca^{2+} within the HAP lattice than it would be for doping to occur at interstitial positions [32, 33]. Furthermore, Ag^{+} substitution would be more likely to maintain the charge balance and lattice stability of HAP relative to interstitial doping [34, 35]. Therefore, we hypothesized that Ag^{+} had probably entered the HAP lattice by substituting for Ca^{2+}.

We then evaluated the chemical constitutions and valence states of the CNT/HAP and CNT/Ag-HAP nanohybrids using XPS (Figs. 1c–1h). Moreover, the spectra of both nanohybrids showed common elements such as C, O, Ca, and P; however, Ag was only found in the CNT/Ag-HAP nanohybrids. This can be seen in Fig. 1d, since the peaks at 368.4 and 374.3 eV corresponded to the binding energies of $Ag3d_{3/2}$ and $Ag3d_{5/2}$, respectively. This confirms the existence of Ag^{+} within the CNT/Ag-HAP nanohybrids [36]. Moreover, we found that the Ca2p and P2p peak-splitting fitting curves for the CNT/Ag-HAP nanohybrids were similar to those for the CNT/HAP nanohybrids, as shown in Figs. 1e–1h. The binding energy peaks at 351.0 and 347.5 eV corresponded to the binding energies of $Ca2p_{1/2}$ and $Ca2p_{3/2}$ of the CNT/Ag-HAP nanohybrids, respectively. Furthermore, the peaks at 133.2 and 134.2 eV were likely attributable to $P2p_{3/2}$ and $P2p_{1/2}$ of the CNT/Ag-HAP nanohybrids, respectively [37]. In comparison with the CNT/HAP nanohybrids, the peaks of the CNT/Ag-HAP nanohybrids shifted toward the lower

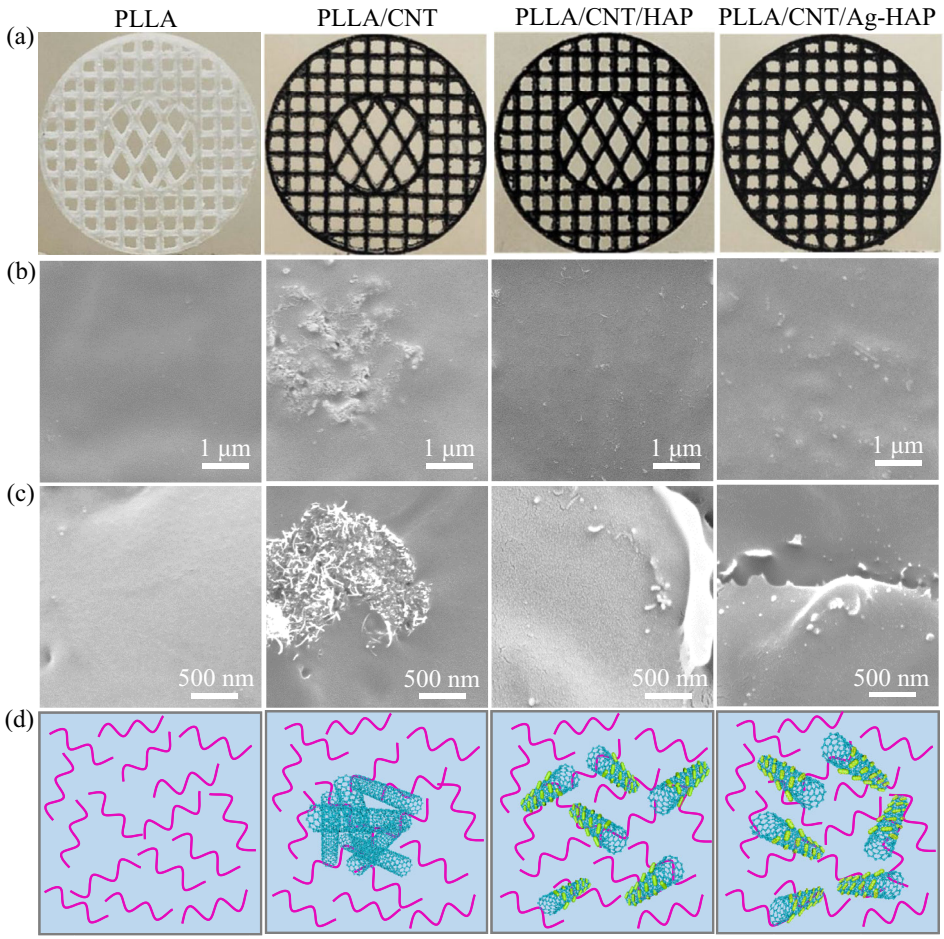

Fig. 4 Fabricated PLLA, PLLA/CNT, PLLA/CNT/HAP, and PLLA/CNT/Ag-HAP scaffolds: **a** digital image, **b** surface morphology, **c** fracture morphology, and **d** schematic of dispersion of the nanohybrids. PLLA: poly-L-lactic acid; CNT: carbon nanotube; HAP: hydroxyapatite; PLLA/CNT/Ag-HAP: Ag-doped CNT/HAP nanohybrids introduced into PLLA

binding energy state. This may have been caused by the doping of Ag^+ into the HAP lattice, thereby leading to lattice strain and eventually structural defects of HAP crystals [38].

Next, the morphology of the CNT/Ag-HAP nanohybrids was studied using SEM. A large number of rod-shaped Ag-HAP nanoparticles are shown in Fig. 2a. More importantly, the CNT/Ag-HAP nanohybrids showed good dispersion. In addition, elements such as Ca, P, and Ag were detected on the surface of CNT/Ag-HAP nanohybrids by EDS in Figs. 2b–2f; this further suggested that Ag-HAP nanoparticles formed on the surfaces of CNT. Further detailed structure of the CNT/Ag-HAP nanohybrids was obtained by TEM imaging (Figs. 2g and 2h). The rod-shaped Ag-HAP nanoparticles were observed on CNT, and the crystal surface spacing was measured at 0.34 and 0.27 nm using the Digital Micrograph software. This corresponds to the interlamellar spacing of the (002) plane in graphite and the identity distance of the (300) plane in HAP, respectively. According to previous studies, the (300) plane of the HAP nanorod can interact with CNT and had a high matching potential. This was largely due to the presence of many carboxyl functional groups along the surfaces of CNTs. In addition, the Ca atoms of HAP could easily match with the O atoms of the carboxyl groups of CNTs, thus forming ionic bonds and even covalent interactions [39–41]. The selected area electron diffraction (SAED) diagram provided in Fig. 2i shows the (201), (300), (322), (302), and (215) planes of HAP, which are representative of HAP planes.

The doping mechanism of the CNT/Ag-HAP nanohybrids is shown in Fig. 3. The presence of abundant surface oxygenic functional groups decorated with carboxyl and epoxide groups on CNTs can provide anchoring sites for the in situ synthesis of HAP nanorods and the partial replacement of Ca^{2+} within the HAP lattice by doped Ag^+ [42]. More specifically, the exposed chelated Ca^{2+}, or Ca^{2+} and Ag^+ on the surface of CNTs, formed ionic bonds with HPO_4^{2-} in solution. This in turn enabled the in situ synthesis of HAP nanorods or Ag-HAP nanohybrids on the surfaces of CNTs in a hydrothermal environment [43].

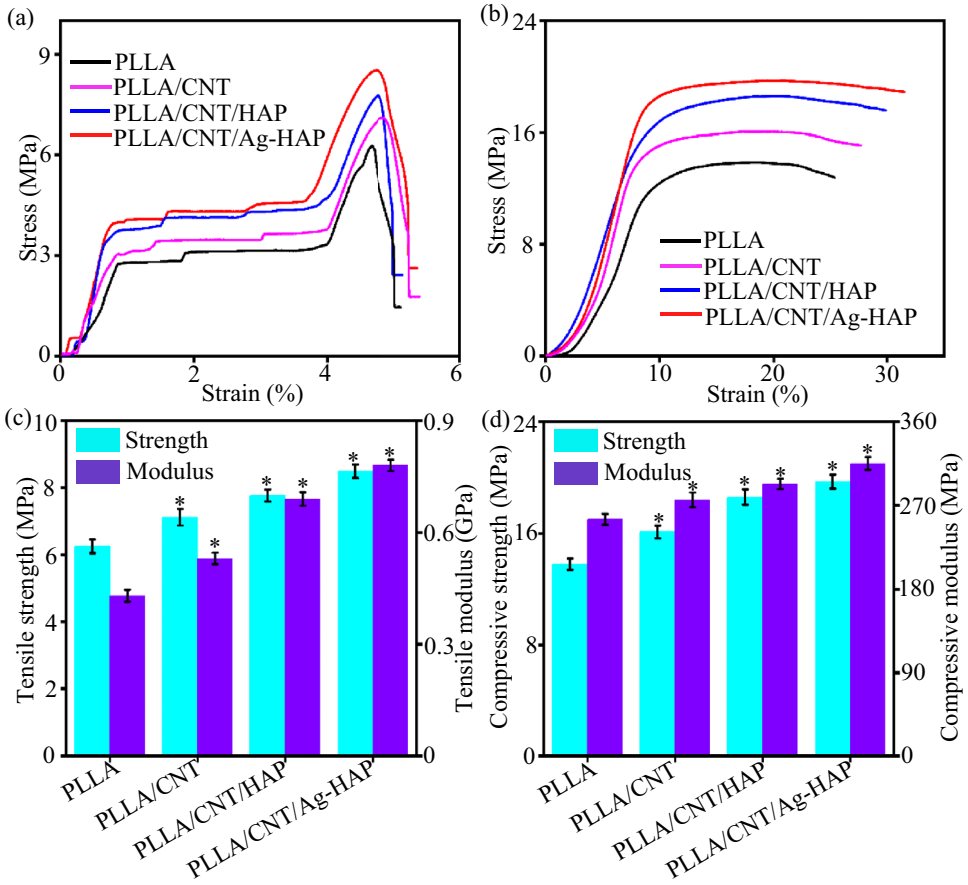

Fig. 5 Mechanical properties of the scaffolds: **a** tensile and **b** compressive stress–strain curves, **c** tensile strength and tensile modulus, and **d** compressive strength and compressive modulus. Data are expressed as mean±standard deviation, n=5, $^{*}p$<0.05. PLLA: poly-L-lactic acid; CNT: carbon nanotube; HAP: hydroxyapatite; PLLA/CNT/Ag-HAP: Ag-doped CNT/HAP nanohybrids introduced into PLLA

Microstructure and mechanical properties

To realize the integration of defect tissue, bone implants should simulate the shape, structure, and function of natural bone to promote proliferation and differentiation of osteoblasts [44, 45]. The PLLA, PLLA/CNT, PLLA/CNT/HAP, and PLLA/CNT/Ag-HAP bone scaffolds, all of which had a porous structure prepared via SLS, are capable of generating custom shapes for bone implants. Digital images of fabricated scaffolds are presented in Fig. 4a, where it can be seen that the porous structure was evenly distributed. This is conducive to supporting the growth of surrounding tissues, promoting blood circulation, and providing a suitable microenvironment for cell proliferation [46, 47]. Meanwhile, the uniform dispersing of nanofillers within the matrix enhances the mechanical properties of the scaffold. We therefore studied the surface and cross-sectional morphologies of the PLLA, PLLA/CNT, PLLA/CNT/HAP, and PLLA/CNT/Ag-HAP scaffolds, as displayed in Figs. 4b and 4c. Compared to the pure PLLA scaffold, we observed visible agglomeration in the PLLA/CNT scaffold, which was mainly due to strong interactions between CNTs subjected to potent van der Waals forces as well as its own π–π bond, leading to aggregation of the PLLA matrix [48, 49]. In contrast, the CNT/HAP and CNT/Ag-HAP nanohybrids presented relatively homogeneous dispersion of the PLLA matrix, probably due to the barrier action of HAP and Ag-HAP on the CNTs, which improved CNT dispersion. Moreover, the CNT/Ag-HAP nanohybrids showed even better dispersion, which may be due to a higher surface negative charge compared to CNT/HAP nanohybrids [50]. Therefore, the co-dispersed nanostructure of the CNT/HAP and CNT/Ag-HAP nanohybrids by in situ synthesis can facilitate the homogeneous dispersion of nanofillers within the PLLA matrix, as shown in Fig. 4d.

Next, tension and compression tests were performed to assess the mechanical properties of the PLLA, PLLA/CNT, PLLA/CNT/HAP, and PLLA/CNT/Ag-HAP scaffolds. These results are shown in Fig. 5. The tensile stress–strain curves of the scaffolds are displayed in Fig. 5a, and the corresponding tensile strength and modulus measurements are shown in Fig. 5c. The tensile strength and modulus of the PLLA/CNT/Ag-HAP scaffold were 8.49 MPa and 0.78 GPa, which were 35.84% and 81.39% higher than the tensile strength and modulus of the PLLA scaffold, respectively.

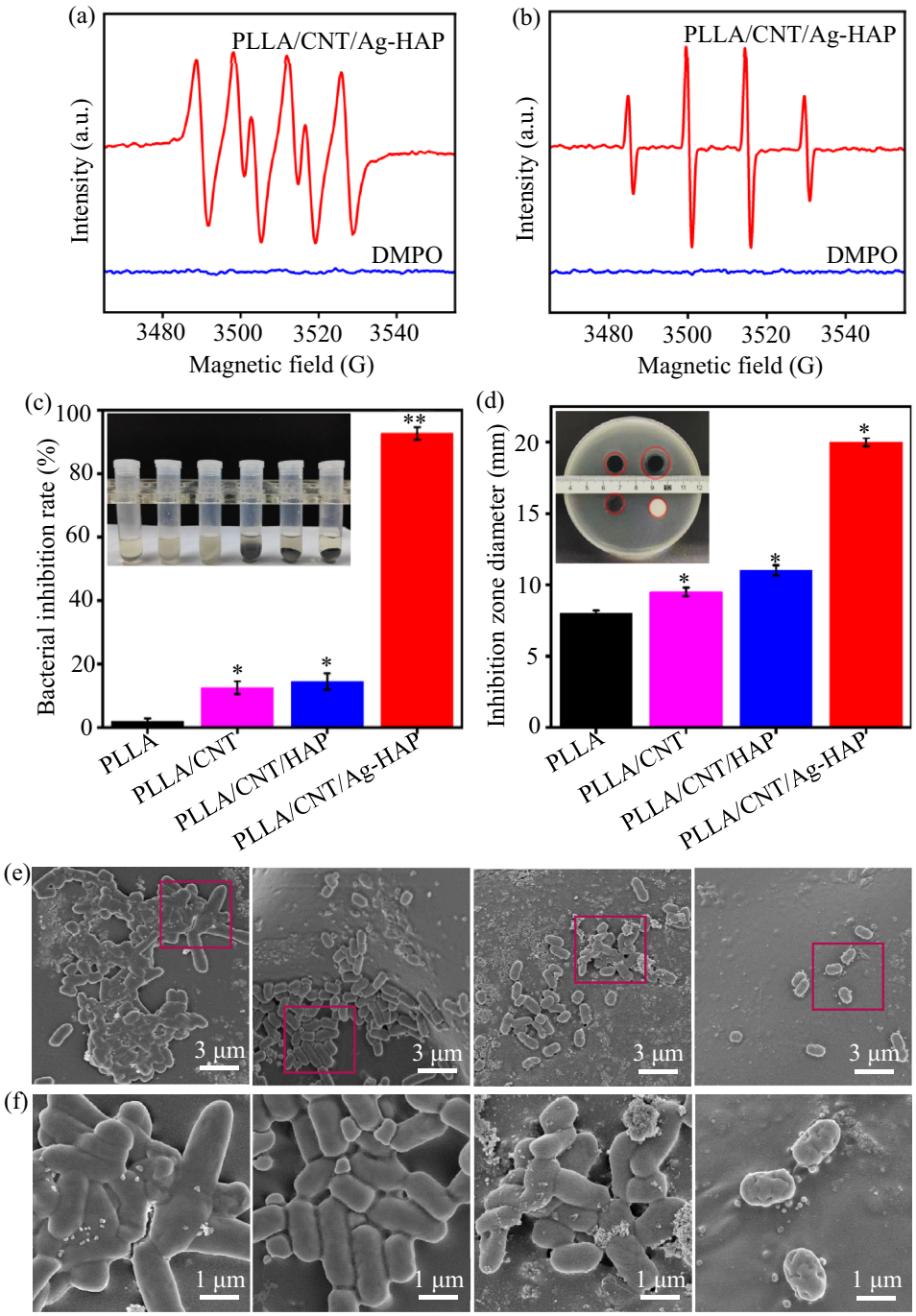

Fig. 6 Antibacterial properties of the scaffolds: EPR spectra of **a** $\cdot O_2^-$ and **b** ·OH generated from the PLLA/CNT/Ag-HAP scaffold, **c** antibacterial rate against *E. coli* (inset: turbidity photograph), **d** the diameter of inhibition zone (inset: photograph of inhibition zone), and **e**, **f** SEM images. Data are expressed as mean±standard deviation, $n = 5$, $^{*}p<0.05$, $^{**}p<0.01$. PLLA: poly-L-lactic acid; CNT: carbon nanotube; HAP: hydroxyapatite; PLLA/CNT/Ag-HAP: Ag-doped CNT/HAP nanohybrids introduced into PLLA; DMPO: 5,5-dimethyl-1-pyrroline-N-oxide; EPR: electron paramagnetic resonance; *E. coli*: *Escherichia coli*; SEM: scanning electron microscopy

These differences are mainly due to the introduction of Ag-HAP nanoparticles, which further optimized the dispersal of CNTs within the PLLA matrix and improved load transport capacity, yielding the observed mechanical enhancement relative to the PLLA scaffold [51]. Measurements of compressive strength and modulus as measured by compressive stress–strain curves were similar to those of tensile properties, and are shown in Figs. 5b and 5d. The compressive strength and modulus of the PLLA/CNT/Ag-HAP scaffold (i.e., 19.72 MPa and 315.03 MPa, respectively) were higher than those of the other scaffolds, and showed an increase of 42.75% and 23.53% compared to the PLLA scaffold. Consequently, the PLLA/CNT/Ag-HAP scaffold showed better mechanical properties than the other scaffolds. It has been previously reported that the dispersion of nanofillers within the matrix was the predominant force impacting scaffold mechanical properties [52]. Moreover, nanofiller dispersion

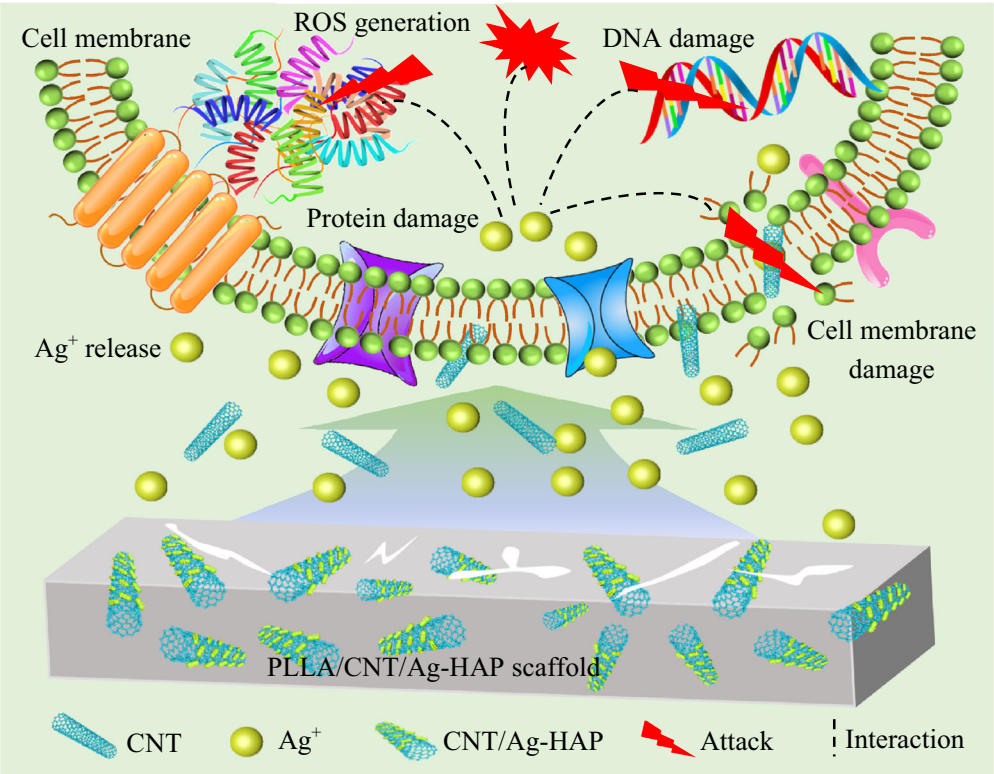

Fig. 7 Diagram showing the antibacterial mechanism of the PLLA/CNT/Ag-HAP scaffold. PLLA: poly-L-lactic acid; CNT: carbon nanotube; HAP: hydroxyapatite; CNT/Ag-HAP: Ag-doped CNT/HAP; PLLA/CNT/Ag-HAP: Ag-doped CNT/HAP nanohybrids introduced into PLLA; ROS: reactive oxygen species

is related to the fact that there is an effective mechanical interlock between the rougher surface of rod-shaped Ag-HAP and the PLLA matrix, and this can further enhance stress transfer effects via interfacial bonding, thereby improving the mechanical properties of scaffolds [40, 53].

Antibacterial properties

Bone scaffolds implanted in the human body can cause bacterial infection and reduce the success rate of surgical interventions, so it is very important to develop bone scaffolds that show sufficient antibacterial activity. In this study, Ag^+ doping was expected to endow scaffolds with antibacterial properties. To verify this hypothesis, we examined the generation of ROS by the PLLA/CNT/Ag-HAP scaffold and conducted turbidimetry and inhibition zone tests of the different scaffolds. As shown in Figs. 6a and 6b, the characteristic signal $\cdot O_2^-$ was observed in the PLLA/CNT/Ag-HAP scaffold, and we also detected typical ·OH spectra with an intensity ratio of 1:2:2:1. These results clearly showed that both $\cdot O_2^-$ and ·OH radicals were generated by the PLLA/CNT/Ag-HAP scaffold, which may be attributed to the fact that the absorption of visible light caused the surface electrons of Ag^+ ions to be excited to higher energy levels. These excited electrons may have then reacted with oxygen molecules in water or solution to generate the $\cdot O_2^-$ and ·OH radicals [54–56]. These results provide preliminary evidence that the PLLA/CNT/Ag-HAP scaffold possesses an endogenous ability to combat bacteria.

The photograph shown in the inset of Fig. 6c was taken during turbidity testing and shows that the turbidity values of bacterial suspensions containing the PLLA, PLLA/CNT, and PLLA/CNT/HAP scaffolds were close to the negative control group. This indicates that they exerted little inhibition of bacterial activity. However, the fluid medium in which the PLLA/CNT/Ag-HAP scaffold was incubated became transparent, thereby indicating that the PLLA/CNT/Ag-HAP scaffold exerted an antibacterial effect that strongly inhibited bacterial growth. Next, the absorbance of the bacterial suspension was qualitatively analyzed using an enzyme-labeling measuring instrument; we found that the antibacterial effects of the PLLA, PLLA/CNT, PLLA/CNT/HAP, and PLLA/CNT/Ag-HAP scaffolds were 2.01%, 12.63%, 14.51%, and 92.65%, respectively (Fig. 6c). The weak

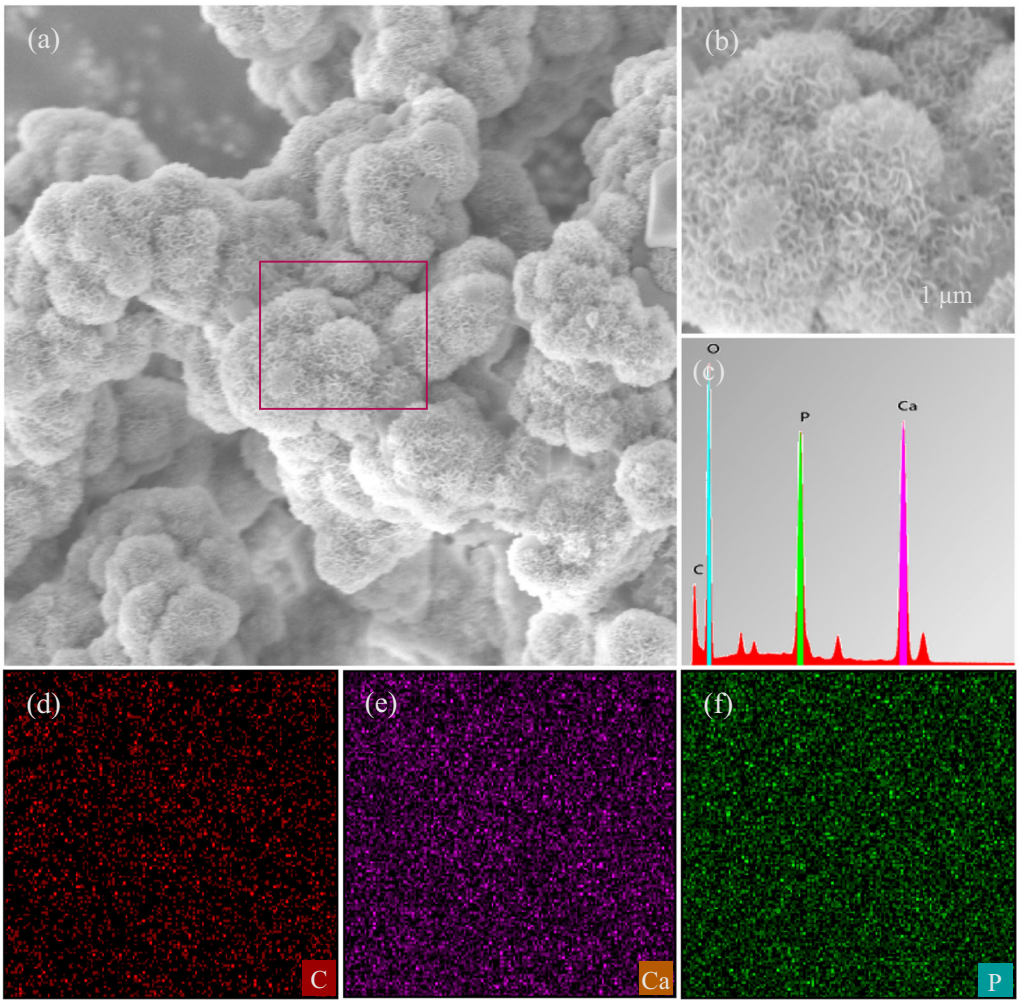

Fig. 8 Mineralization ability of the PLLA/CNT/Ag-HAP scaffold: **a** SEM image and **b** the corresponding local magnification, **c** EDS mapping spectra analysis, and **d**–**f** distribution of C, Ca, and P following SBF immersion for 28 d. PLLA: poly-L-lactic acid; CNT: carbon nanotube; HAP: hydroxyapatite; PLLA/CNT/Ag-HAP: Ag-doped CNT/HAP nanohybrids introduced into PLLA; SEM: scanning electron microscopy; EDS: energy-dispersive spectrometer; SBF: simulated body fluid

antibacterial effects of the PLLA/CNT and PLLA/CNT/HAP scaffolds were probably due to the high aspect ratio of CNTs. This may have given it the ability to penetrate cells, thus increasing the transmembrane permeability, reducing the bacterial metabolic activity, and ultimately leading to bacterial death [57, 58]. In contrast, the PLLA/CNT/Ag-HAP scaffold showed a strong antibacterial effect (i.e., 92.65%), indicating that a large majority of *E. coli* cells were killed. Next, the results of the inhibition zone test are shown in Fig. 6d. Here, the larger the diameter of the inhibition zone, the stronger the antibacterial effect [59]. Compared to the other scaffolds, the PLLA/CNT/Ag-HAP scaffold possessed a significantly larger inhibition zone, with its diameter increasing from 8 to 20 mm. The morphology of bacteria on the scaffolds was then observed by SEM, as shown in Figs. 6e and 6f. We found that many coryneform and smooth-surfaced *E. coli* cells adhered to the surface of the PLLA, PLLA/CNT, and PLLA/CNT/HAP scaffolds under standard growth conditions. However, very few *E. coli* cells were present on the PLLA/CNT/Ag-HAP scaffold, and they showed abnormal cell morphology, exhibiting holes and depressions and loss of membrane integrity. This finding suggests that the PLLA/CNT/Ag-HAP scaffold possesses a strong antibacterial effect via acting to inhibit bacterial adhesion and destroy bacterial membrane integrity.

Taken together, these results indicate that the PLLA/CNT/Ag-HAP scaffold possesses significant antibacterial activity, which can be attributed to Ag^{+} doping. The possible antibacterial mechanism by which the PLLA/CNT/Ag-HAP scaffold acts against *E. coli* is shown

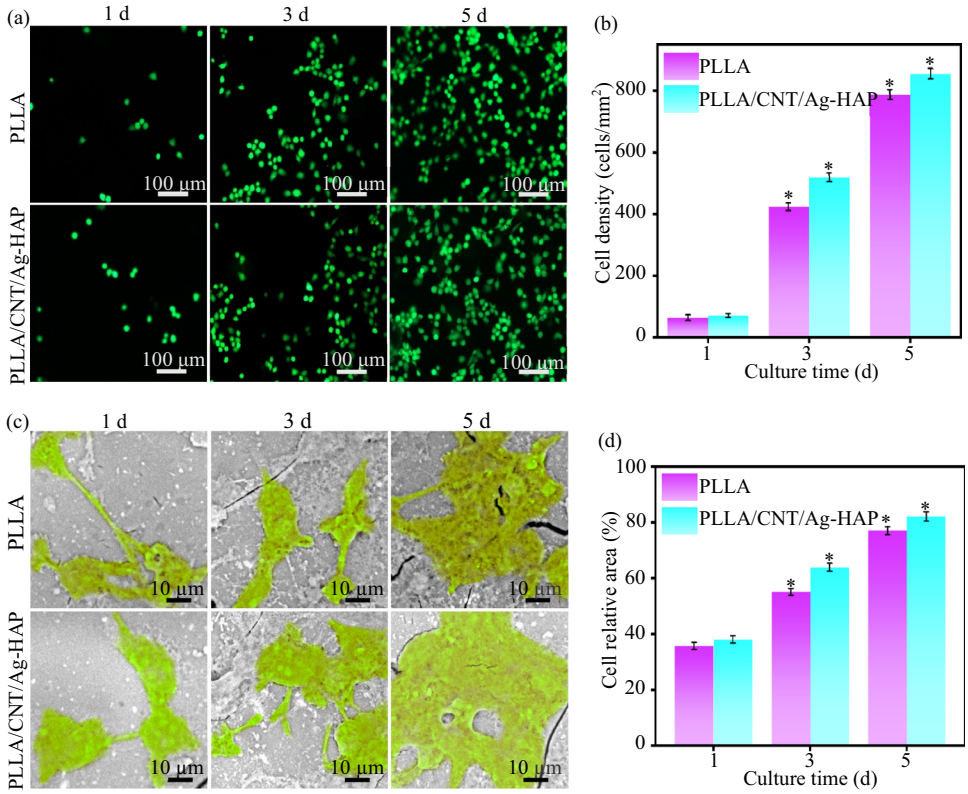

Fig. 9 Cytocompatibility of the PLLA/CNT/Ag-HAP scaffold: **a** fluorescence images of live and dead cells cultivated on the PLLA and PLLA/CNT/Ag-HAP scaffolds for 1, 3, and 5 d, **b** statistical analysis of live cell density, **c** adhesion morphologies of cells cultivated on the PLLA and PLLA/CNT/Ag-HAP scaffolds for 1, 3, and 5 d, and **d** corresponding statistical analysis of cell relative areas. Data are expressed as mean±standard deviation, n=5, $^{*}p$<0.05. PLLA: poly-L-lactic acid; CNT: carbon nanotube; HAP: hydroxyapatite; PLLA/CNT/Ag-HAP: Ag-doped CNT/HAP nanohybrids introduced into PLLA

in Fig. 7. Briefly, Ag^+ is slowly released during the degradation of the PLLA/CNT/Ag-HAP scaffold. These released Ag^+ ions then bind to negatively charged bacterial cell membranes via the electrostatic effect and then interact with the SH group of membrane proteins. This alters membrane permeability and disrupts membrane integrity. Moreover, Ag^+ with high catalytic capacity and reduction potential can destroy the respiratory chain of *E. coli*, thus producing additional ROS, which possess strong oxidizing property. Moreover, highly reactive Ag^+ and ROS can disrupt the molecular structure of bacterial DNA, thereby inhibiting mRNA replication and deactivating protein function [60]. At the same time, CNTs have sharp edges and physically interact with *E. coli* to destroy the bacterial cell membrane, thereby facilitating Ag^+ transport across the cell membrane [61]. Taken together, these actions can disrupt the multiplication and survival of *E. coli*, and thereby endow the PLLA/CNT/Ag-HAP scaffold with a strong antibacterial effect.

Bioactivity and cytocompatibility

Good bioactivity is a key determinant of good integration of bone scaffolds into human bone [62]. Research has suggested that the ability of biomaterials to form an apatite layer following immersion in SBF can predict their bioactivity in vivo [63]. Therefore, the mineralization behavior of the PLLA/CNT/Ag-HAP scaffold was evaluated using an immersion test in SBF. In addition, the surface morphology and the distribution of relevant elements of the scaffold were examined using SEM and EDS, respectively. A large number of clustered particles deposited on the PLLA/CNT/Ag-HAP scaffold are shown in Figs. 8a and 8b. These particles were primarily composed of C, O, Ca, and P, as shown in Figs. 8c–8f, and show a Ca/P ratio of approximately 1.65, which is similar to apatite [64]. Therefore, it is reasonable to infer that apatite was deposited on the PLLA/CNT/Ag-HAP scaffold, and the in vitro mineralization activity of the PLLA/CNT/Ag-HAP scaffold increased in the presence of the CNT/Ag-HAP nanohybrids. There are several possible reasons for this. On the one hand, CNTs possess numerous negatively charged functional groups that can attract Ca^{2+} and facilitate the formation of apatite. On the other hand, Ca^{2+} and HPO_4^{2-} released by the PLLA/CNT/Ag-HAP scaffold may contribute to the local supersaturation of the solution, thus accelerating the deposition of apatite on the scaffold.

Good cytocompatibility is a basic requirement for using artificial bone scaffolds as bone implants [65, 66]. Given

the superior mechanical, antibacterial, and bioactivity properties of the PLLA/CNT/Ag-HAP scaffold, we selected the PLLA/CNT/Ag-HAP scaffold to evaluate the cytocompatibility; here we used the PLLA scaffold as the control group. First, cell viability on the scaffolds was detected using fluorescence staining experiments, and all living cells that exhibited green fluorescence are shown in Fig. 9a. Most MG63 cells exhibited a spherical morphology and were attached to the scaffolds after 1 d of culture. As the culture time prolonged, these cells continued to grow and spread. After 5 d of culture, the number of cells increased, and filopodia began to appear. The quantity of MG63 cells cultivated on the PLLA/CNT/Ag-HAP scaffold was higher and their morphological features were more obvious compared to those on the PLLA scaffold, as shown in Fig. 9b. Furthermore, the cell adhesion morphology of the scaffolds was observed, as shown in Fig. 9c. After 1 d of culture, cells attached to the scaffolds showed a fusiform appearance with platelike pseudopods surrounding them. After 5 d, the filamentous pseudopodia of the cells gradually extended to cover most of the scaffold. Compared to the PLLA scaffold, the PLLA/CNT/Ag-HAP scaffold exhibited a higher number of adherent cells and a larger area of spreading during the trial period. Taken together, the results of these cell experiments show that the addition of the CNT/Ag-HAP nanohybrids was conducive to the promotion of cell adhesion and proliferation. This was due to the good bioactivity of the PLLA/CNT/Ag-HAP scaffold, the production of an apatite layer on its surface, and its similarity to the composition of natural bone [44].

Conclusions

In this study, CNT/Ag-HAP nanohybrids were synthesized by using Ag^+ doping to partially replace the Ca^{2+} in HAP lattice grown in situ on CNTs. Here, rod-shaped Ag-HAP nanoparticles were homogeneously dispersed on CNTs. After synthesis, CNT/Ag-HAP nanohybrids were introduced into the PLLA matrix, and the resulting PLLA/CNT/Ag-HAP scaffold was found to have good mechanical properties, antibacterial properties, bioactivity, and cytocompatibility. In addition, the results of antibacterial experiments indicated that the PLLA/CNT/Ag-HAP scaffold possessed efficient antibacterial properties, as it was able to kill 92.65% of *E. coli* cells it was exposed to. This antibacterial function was attributed to the sustained release of doped Ag^+, which is highly catalytic. This release likely damaged bacterial cell membranes through electrostatic adsorption, thereby destroying DNA structures and causing a rapid loss of protease activity. These effects resulted in the death of many bacteria. Finally, we note that the mechanical properties, bioactivity, and cytocompatibility of the PLLA/CNT/Ag-HAP scaffold were all optimized relative to the PLLA scaffold.

Acknowledgements This work was supported by the following funds: (1) the National Natural Science Foundation of China (Nos. 52275393 and 51935014); (2) Hunan Provincial Natural Science Foundation of China (Nos. 2021JJ20061, 2020JJ3047, and 2019JJ50588); (3) Jiangxi Provincial Natural Science Foundation of China (No. 20224ACB204013); (4) the Project of State Key Laboratory of High Performance Complex Manufacturing; (5) Technology Innovation Platform Project of Shenzhen Institute of Information Technology 2020 (No. PT2020E002); (6) Guangdong Province Precision Manufacturing and Intelligent Production Education Integration Innovation Platform (No. 2022CJPT019); and (7) Independent Exploration and Innovation Project of Central South University (No. 1053320220553). The authors would like to thank eceshi (www.eceshi.com) for the ICP-AES/MS test and Shiyanjia Lab (www.shiyanjia.com) for the EPR analysis.

Author contributions CJS and XXS were involved in conceptualization, investigation, writing—original draft; KW and YLG were involved in visualization and resources; KW and FY helped in writing—review & editing; and PF contributed to supervision.

Declarations

Conflict of interest CJS is an associate editor for *Bio-Design and Manufacturing* and was not involved in the editorial review or the decision to publish this article. The authors declare that they have no conflict of interest.

Ethical approval This article does not contain any studies with human or animal subjects performed by any of the authors.

References

1. Dang HP, Shabab T, Shafiee A et al (2019) 3D printed dual macro-, microscale porous network as a tissue engineering scaffold with drug delivering function. Biofabrication 11(3):035014. https://doi.org/10.1088/1758-5090/ab14ff
2. Kalsi S, Singh J, Sehgal SS et al (2021) Biomaterials for tissue engineered bone scaffolds: a review. Mater Today Proc 81(2):888–893. https://doi.org/10.1016/j.matpr.2021.04.273
3. Feng P, Zhao RY, Tang WM et al (2023) Structural and functional adaptive artificial bone: materials, fabrications, and properties. Adv Funct Mater 33(23):2214726. https://doi.org/10.1002/adfm.202214726
4. Shao HF, Nian ZH, Jing ZL et al (2022) Additive manufacturing of hydroxyapatite bioceramic scaffolds with projection based 3D printing. Chin J Mech Eng Addit Manuf Front 1(2):100021. https://doi.org/10.1016/j.cjmeam.2022.100021
5. Esmi A, Jahani Y, Yousefi AA et al (2019) PMMA-CNT-HAP nanocomposites optimized for 3D-printing applications. Mater Res Express 6(8):085405. https://doi.org/10.1088/2053-1591/ab2157
6. Zhang L, Yang GJ, Johnson BN et al (2019) Three-dimensional (3D) printed scaffold and material selection for bone repair. Acta Biomater 84:16–33. https://doi.org/10.1016/j.actbio.2018.11.039
7. Qi F, Wang Z, Yang L et al (2023) A collaborative CeO_2@metal-organic framework nanosystem to endow scaffolds with photodynamic antibacterial effect. Mater Today Chem 27:101336. https://doi.org/10.1016/j.mtchem.2022.101336

8. Qian GW, Zhang LM, Shuai Y et al (2023) 3D-printed $CuFe_2O_4$-MXene/PLLA antibacterial tracheal scaffold against implantation-associated infection. Appl Surf Sci 614:156108. https://doi.org/10.1016/j.apsusc.2022.156108
9. Yang CS, Zhou L, Geng XD et al (2022) New dual-function in situ bone repair scaffolds promote osteogenesis and reduce infection. J Biol Eng 16(1):23. https://doi.org/10.1186/s13036-022-00302-y
10. Wu YZ, Liao Q, Wu L et al (2021) ZnL_2-BPs integrated bone scaffold under sequential photothermal mediation: a win–win strategy delivering antibacterial therapy and fostering osteogenesis thereafter. ACS Nano 15(11):17854–17869. https://doi.org/10.1021/acsnano.1c06062.s001
11. Zan J, Shuai Y, Zhang J et al (2023) Hyaluronic acid encapsulated silver metal organic framework for the construction of a slow-controlled bifunctional nanostructure: antibacterial and anti-inflammatory in intrauterine adhesion repair. Int J Biol Macromol 230:123361. https://doi.org/10.1016/j.ijbiomac.2023.123361
12. Agnihotri R, Gaur S, Albin S (2020) Nanometals in dentistry: applications and toxicological implications—a systematic review. Biol Trace Elem Res 197(1):70–88. https://doi.org/10.1007/s12011-019-01986-y
13. Feng P, Shen SP, Shuai Y et al (2023) PLLA grafting draws GO from PGA phase to the interface in PLLA/PGA bone scaffold owing enhanced interfacial bonding. Sustain Mater Technol 35:e00566. https://doi.org/10.1016/j.susmat.2023.e00566
14. Riaz M, Zia R, Ijaz A et al (2018) Synthesis of monophasic Ag doped hydroxyapatite and evaluation of antibacterial activity. Mater Sci Eng C 90:308–313. https://doi.org/10.1016/j.msec.2018.04.076
15. Uskoković V (2020) Ion-doped hydroxyapatite: an impasse or the road to follow? Ceram Int 46(8):11443–11465. https://doi.org/10.1016/j.ceramint.2020.02.001
16. Mansour SF, El-Dek SI, Dorozhkin SV et al (2017) Physico-mechanical properties of Mg and Ag doped hydroxyapatite/chitosan biocomposites. New J Chem 41(22):13773–13783. https://doi.org/10.1039/c7nj01777d
17. Sobczak-Kupiec A, Pluta K, Drabczyk A et al (2018) Synthesis and characterization of ceramic-polymer composites containing bioactive synthetic hydroxyapatite for biomedical applications. Ceram Int 44(12):13630–13638. https://doi.org/10.1016/j.ceramint.2018.04.199
18. Li XJ, Yuan Y, Liu LY et al (2020) 3D printing of hydroxyapatite/tricalcium phosphate scaffold with hierarchical porous structure for bone regeneration. Bio-Des Manuf 3(1):15–29. https://doi.org/10.1007/s42242-019-00056-5
19. Mohiti-Asli M, Pourdeyhimi B, Loboa EG (2014) Novel, silver-ion-releasing nanofibrous scaffolds exhibit excellent antibacterial efficacy without the use of silver nanoparticles. Acta Biomater 10(5):2096–2104. https://doi.org/10.1016/j.colsurfb.2019.01.064
20. Yang YW, Cheng Y, Deng F et al (2021) A bifunctional bone scaffold combines osteogenesis and antibacterial activity via in situ grown hydroxyapatite and silver nanoparticles. Bio-Des Manuf 4(3):452–468. https://doi.org/10.1007/s42242-021-00130-x
21. Karunakaran G, Cho EB, Kumar GS et al (2019) Ascorbic acid-assisted microwave synthesis of mesoporous Ag-doped hydroxyapatite nanorods from biowaste seashells for implant applications. ACS Appl Bio Mater 2(5):2280–2293. https://doi.org/10.1021/acsabm.9b00239
22. Karthieka RR, Prakash T (2023) Influence of applied bias on direct conversion X-ray sensing capability of nanocrystalline $Ca_9Ag(PO_4)_6(OH)_2$. Mater Sci Semicond Process 162:107517. https://doi.org/10.1016/j.mssp.2023.107517
23. Jin S, Li JD, Wang J et al (2018) Electrospun silver ion-loaded calcium phosphate/chitosan antibacterial composite fibrous membranes for guided bone regeneration. Int J Nanomed 13:4591–4605. https://doi.org/10.2147/IJN.S167793
24. Dong Y, Chen AN, Yang T et al (2023) Microstructure evolution and mechanical properties of Al_2O_3 foams via laser powder bed fusion from Al particles. Adv Powder Mater 2(4):100135. https://doi.org/10.1016/j.apmate.2023.100135
25. Tian XY, Wu LL, Gu DD et al (2022) Roadmap for additive manufacturing: toward intellectualization and industrialization. Chin J Mech Eng Addit Manuf Front 1(1):100014. https://doi.org/10.1016/j.cjmeam.2022.100014
26. Niu PD, Li RD, Fan ZQ et al (2023) Inhibiting cracking and improving strength for additive manufactured $Al_xCoCrFeNi$ high entropy alloy via changing crystal structure from BCC-to-FCC. Addit Manuf 71:103584. https://doi.org/10.1016/j.addma.2023.103584
27. Chen AN, Su J, Li YJ et al (2023) 3D/4D printed bio-piezoelectric smart scaffolds for next-generation bone tissue engineering. Int J Extreme Manuf 5:032007. https://doi.org/10.1088/2631-7990/acd88f
28. Gao CD, Yao X, Deng YW et al (2023) Laser-beam powder bed fusion followed by annealing with stress: a promising route for magnetostrictive improvement of polycrystalline $Fe_{81}Ga_{19}$ alloys. Addit Manuf 68:103516. https://doi.org/10.1016/j.addma.2023.103516
29. Ji HR, Zhao MC, Xie B et al (2021) Corrosion and antibacterial performance of novel selective-laser-melted (SLMed) Ti-xCu biomedical alloys. J Alloy Comp 864:158415. https://doi.org/10.1016/j.jallcom.2020.158415
30. Hassan AA, Radwan HA, Abdelaal SA et al (2021) Polycaprolactone based electrospun matrices loaded with Ag/hydroxyapatite as wound dressings: morphology, cell adhesion, and antibacterial activity. Int J Pharmaceut 593:120143. https://doi.org/10.1016/j.ijpharm.2020.120143
31. Esfahani H, Salahi E, Tayebifard A et al (2014) Influence of zinc incorporation on microstructure of hydroxyapatite to characterize the effect of pH and calcination temperatures. J Asian Ceram Soc 2(3):248–252. https://doi.org/10.1016/j.jascer.2014.05.001
32. Nikolova V, Kircheva N, Dobrev S et al (2023) Lanthanides as calcium mimetic species in calcium-signaling/buffering proteins: the effect of lanthanide type on the Ca^{2+}/Ln^{3+} competition. Int J Mol Sci 24(7):6297. https://doi.org/10.3390/ijms24076297
33. Saini RK, Bagri LP, Bajpai A (2019) Nano-silver hydroxyapatite based antibacterial 3D scaffolds of gelatin/alginate/poly(vinyl alcohol) for bone tissue engineering applications. Colloids Surf B 177:211–218. https://doi.org/10.1016/j.colsurfb.2019.01.064
34. Nagyne-Kovacs T, Meszaros B, Molnar M et al (2020) Hydrothermal synthesis of Sr-doped hydroxyapatite and its antibacterial activity. Period Polytech Chem Eng 64(1):54–60. https://doi.org/10.3311/PPch.14062
35. Jacobs A, Gaulier M, Duval A et al (2019) Silver doping mechanism in bioceramics—from Ag^+:doped HAp to Ag°/BCP nanocomposite. Crystals 9(7):326. https://doi.org/10.3390/cryst9070326
36. Wang JR, Gong X, Hai J et al (2018) Synthesis of silver–hydroxyapatite composite with improved antibacterial properties. Vacuum 152:132–137. https://doi.org/10.1016/j.vacuum.2018.03.015
37. Ciobanu CS, Iconaru SL, Pasuk I et al (2013) Structural properties of silver doped hydroxyapatite and their biocompatibility. Mater Sci Eng C 33(3):1395–1402. https://doi.org/10.1016/j.msec.2012.12.042
38. Maleki-Ghaleh H, Siadati MH, Fallah A et al (2021) Effect of zinc-doped hydroxyapatite/graphene nanocomposite on the physicochemical properties and osteogenesis differentiation of 3D-printed polycaprolactone scaffolds for bone tissue engineering. Chem Eng J 426:131321. https://doi.org/10.1016/j.cej.2021.131321
39. Li HP, Song XQ, Li BE et al (2017) Carbon nanotube-reinforced mesoporous hydroxyapatite composites with excellent mechanical

and biological properties for bone replacement material application. Mater Sci Eng C 77:1078–1087. https://doi.org/10.1016/j.msec.2017.04.048
40. Khan AS, Hussain AN, Sidra L et al (2017) Fabrication and in vivo evaluation of hydroxyapatite/carbon nanotube electrospun fibers for biomedical/dental application. Mater Sci Eng C 80:387–396. https://doi.org/10.1016/j.msec.2017.05.109
41. Im YO, Lee SH, Kim T et al (2017) Utilization of carboxylic functional groups generated during purification of carbon nanotube fiber for its strength improvement. Appl Surf Sci 392:342–349. https://doi.org/10.1016/j.apsusc.2016.09.060d
42. Afroze JD, Abden MJ, Alam MS et al (2016) Development of functionalized carbon nanotube reinforced hydroxyapatite magnetic nanocomposites. Mater Lett 169:24–27. https://doi.org/10.1016/j.matlet.2016.01.060
43. Guo WT, Wang XC, Yang CY et al (2022) Microfluidic 3D printing polyhydroxyalkanoates-based bionic skin for wound healing. Mater Future 1(1):015401. https://doi.org/10.1088/2752-5724/ac446b
44. Feng JW, Fu JZ, Yao XH et al (2022) Triply periodic minimal surface (TPMS) porous structures: from multi-scale design, precise additive manufacturing to multidisciplinary applications. Int J Extreme Manuf 4(2):022001. https://doi.org/10.1088/2631-7990/ac5be6
45. Li QT, Xu S, Feng Q et al (2021) 3D printed silk-gelatin hydrogel scaffold with different porous structure and cell seeding strategy for cartilage regeneration. Bioact Mater 6(10):3396–3410. https://doi.org/10.1016/j.bioactmat.2021.03.013
46. Han W, Kong LB, Xu M (2022) Advances in selective laser sintering of polymers. Int J Extreme Manuf 4(4):042002. https://doi.org/10.1088/2631-7990/ac9096
47. Chen XM, Zhang LY, Zheng M et al (2015) Quantitative nanomechanical characterization of the van der Waals interfaces between carbon nanotubes and epoxy. Carbon 82:214–228. https://doi.org/10.1016/j.carbon.2014.10.065
48. Zhao Y, Qiu YH, Fang ZX et al (2022) Preparation and characterization of Sr-substituted hydroxyapatite/reduced graphene oxide 3D scaffold as drug carrier for alendronate sodium delivery. Ceram Int 48(24):36601–36608. https://doi.org/10.1016/j.ceramint.2022.08.219
49. Gupta N, Gupta SM, Sharma SK (2019) Carbon nanotubes: synthesis, properties and engineering applications. Carbon Lett 29(5):419–447. https://doi.org/10.1007/s42823-019-00068-2
50. Sezer HK, Eren OM (2019) FDM 3D printing of MWCNT reinforced ABS nano-composite parts with enhanced mechanical and electrical properties. J Manuf Process 37:339–347. https://doi.org/10.1016/j.jmapro.2018.12.004
51. Li PB, Tan WT, Gao MM et al (2021) Strengthening of the magnesium matrix composites hybrid reinforced by chemically oxidized carbon nanotubes and in situ Mg_2Si_p. J Alloys Compd 858:157673. https://doi.org/10.1016/j.jallcom.2020.157673
52. Jaswal R, Shrestha S, Shrestha BK et al (2020) Nanographene enfolded AuNPs sophisticatedly synchronized polycaprolactone based electrospun nanofibre scaffold for peripheral nerve regeneration. Mater Sci Eng C 116:111213. https://doi.org/10.1016/j.msec.2020.111213
53. Sukhorukova IV, Sheveyko AN, Shvindina NV et al (2017) Approaches for controlled Ag^+ ion release: influence of surface topography, roughness, and bactericide content. ACS Appl Mater Interfaces 9(4):4259–4271. https://doi.org/10.1021/acsami.6b15096
54. Shi J, Wang J, Liang LB et al (2021) Carbothermal synthesis of biochar-supported metallic silver for enhanced photocatalytic removal of methylene blue and antimicrobial efficacy. J Hazard Mater 401:123382. https://doi.org/10.1016/j.jhazmat.2020.123382
55. Qin ZJ, Zheng YK, Wang YH et al (2021) Versatile roles of silver in Ag-based nanoalloys for antibacterial applications. Coord Chem Rev 449:214218. https://doi.org/10.1016/j.ccr.2021.214218
56. Webster RD (2023) Electrochemistry combined with electron paramagnetic resonance (EPR) spectroscopy for studying catalytic and energy storage processes. Curr Opin Electrochem 40:101308. https://doi.org/10.1016/j.coelec.2023.101308
57. Shukla AK, Alam J, Ansari MA et al (2019) Selective ion removal and antibacterial activity of silver-doped multi-walled carbon nanotube/polyphenylsulfone nanocomposite membranes. Mater Chem Phys 233:102–112. https://doi.org/10.1016/j.matchemphys.2019.05.054
58. Qian GW, Wang JZ, Yang LM et al (2023) A pH-responsive CaO_2@ZIF-67 system endows a scaffold with chemodynamic therapy properties. J Mater Sci 58(3):1214–1228. https://doi.org/10.1007/s10853-022-08103-w
59. Jayaramudu T, Varaprasad K, Reddy KK et al (2020) Chitosan-pluronic based Cu nanocomposite hydrogels for prototype antimicrobial applications. Int J Biol Macromol 143:825–832. https://doi.org/10.1016/j.ijbiomac.2019.09.143
60. Kung ML, Tai MH, Lin PY et al (2017) Silver decorated copper oxide (Ag@CuO) nanocomposite enhances ROS-mediated bacterial architecture collapse. Colloids Surf B 155(1):399–407. https://doi.org/10.1016/j.colsurfb.2017.04.041
61. Xin Q, Shah H, Nawaz A et al (2019) Antibacterial carbon-based nanomaterials. Adv Mater 31(45):1804838. https://doi.org/10.1002/adma.201804838
62. Oladapo BI, Zahedi SA, Adeoye AOM (2019) 3D printing of bone scaffolds with hybrid biomaterials. Compos Part B Eng 158:428–436. https://doi.org/10.1016/j.compositesb.2018.09.065
63. Zadpoor AA (2014) Relationship between in vitro apatite-forming ability measured using simulated body fluid and in vivo bioactivity of biomaterials. Mater Sci Eng C 35(1):134–143. https://doi.org/10.1016/j.msec.2013.10.026
64. Diogo GS, Marques CF, Freitas-Ribeiro S et al (2022) Mineralized collagen as a bioactive ink to support encapsulation of human adipose stem cells: a step towards the future of bone regeneration. Biomater Adv 133:112600. https://doi.org/10.1016/j.msec.2021.112600
65. Qi FW, Liao RB, Wu P et al (2023) An electrical microenvironment constructed based on electromagnetic induction stimulates neural differentiation. Mater Chem Front 7(8):1671–1683. https://doi.org/10.1039/d2qm01193j
66. Lee SH, Lee KG, Lee J et al (2023) Three-dimensional kagome structures in a PCL/HA-based hydrogel scaffold to lead slow BMP-2 release for effective bone regeneration. Bio-Des Manuf 6(1):12–25. https://doi.org/10.1007/s42242-022-00219-x